Bulletin of Earthquake Engineering (2023) 21:1577–1598
https://doi.org/10.1007/s10518-022-01514-9

S.I. : ADVANCES ON INERTER-BASED SEISMIC PROTECTION OF STRUCTURES

Performance of structures with clutch inerter dampers subjected to seismic excitation

Peter C. Talley[1] · Anika T. Sarkar[1] · Nicholas E. Wierschem[1] · Mark D. Denavit[1]

Received: 15 October 2021 / Accepted: 5 September 2022 / Published online: 19 September 2022

Abstract

Inerter-based passive control devices have great potential to efficiently mitigate damage to structures subjected to earthquakes as they can provide large added mass effects, while having a relatively small physical mass. The added mass effect of inerters is typically achieved through the conversion of translational motion to the rotation of a flywheel. In a clutch inerter damper (CID), energy transferred to the flywheel cannot transfer back to the structure. Despite this potentially advantageous behavior, few studies have considered the seismic performance of structures with CIDs. As a result, the effect of the device parameters (i.e., effective mass and damping), the ability of the device to delay yielding and collapse of the structure, and the relative effectiveness of the device in far-field and near-field earthquakes, which more often include a dominant pulse, are uncertain. This paper addresses these gaps in knowledge through a numerical study of SDOF structures. The numerical model considers the nonlinear behavior of the structure in addition to nonlinear behavior of the CID. Incremental dynamic analyses were performed with suites of recorded earthquake ground motions. The results of these analyses showed that the CID is typically significantly more effective than a comparable viscous damper. Also, while performance differences were observed for different earthquake types, the median performance is broadly similar. Overall, this work shows the CID is capable of delaying the onset of yielding and collapse and otherwise mitigating the effects of a wide range of types of seismic excitation; thus, further investigation on its use is warranted.

Keywords Inerter · Clutch · Damper · Seismic · Nonlinear

✉ Nicholas E. Wierschem
nwiersch@utk.edu

[1] Department of Civil and Environmental Engineering, The University of Tennessee, Knoxville, TN, USA

1 Introduction

Passive control of structures can mitigate damage and other losses from earthquakes. Conventional passive control strategies include the use of viscous dampers, friction dampers, base isolation systems, and tuned mass dampers. Newer devices that include inerters have shown great potential in recent research and practical applications. Inerters are two-terminal mechanical elements that can create large mass effects. The motion of the inerter generates a reaction force that is proportional to the relative acceleration between its terminals (Smith 2002). The proportionality constant of the inerter is referred to as inertance. Inertance is often produced by using a rack and pinion or ball screw to transform translational motion to the rotational motion of a flywheel. However, inertance can also be produced through other means including hydraulic or electro-magnetic-based mechanisms (Ma et al. 2021; Smith 2020; Wagg 2021). As an example of the potential for large mass effects with inerters, Sugimura et al. described a large inerter-based device that is currently in service in a building in Japan. The device can produce 5,400,000 kg of effective mass utilizing a flywheel with a physical mass of 560 kg, resulting in a mass amplification factor of 9600 (Sugimura et al. 2012).

Extensive research has been conducted on inerter-based vibration control devices in the field of civil engineering. As inerter-based devices have a significant mass amplification effect, they have been investigated as a means of enhancing the performance of tuned mass dampers (Garrido et al. 2013; Ikago et al. 2012; Javidialesaadi and Wierschem 2019; Lazar et al. 2014). Researchers have also investigated directly integrating devices with inerters into systems for the vibration control of structures. Often, the inerter-based devices considered in structures have configurations featuring the parallel or series connection of a spring, damper, and inerter as outlined by Hu and Chen (2015). An example of an inerter-based device used in an inter-story capacity is provided by Hwang et al. who investigated a rotational inertia damper in connection with toggle braces to control the vibration of building structures (Hwang et al. 2007). Researchers have also investigated including inerter-based devices as part of building isolation systems (Wang et al. 2010; Zhao et al. 2021). Furthermore, inerter-based devices have been investigated when incorporated into specialized structural systems, such as rocking walls (Di Egidio et al. 2021) and outriggers (Asai and Watanabe 2017).

A related damping device called a clutch inerter damper (CID) was proposed by Makris and Kampas (2016). This device uses two parallel rotational inertia systems with a clutch such that the device can mitigate the response of a structure by permanently dissipating the stored energy in the rotating flywheels. Makris and Kampas demonstrated that the CID effectively reduces the spectral displacements of long period single-degree-of-freedom (SDOF) structures (Makris and Kampas 2016).

Wang and Sun made further efforts to understand the damping behavior of the CID compared to the inertial mass damper (Wang and Sun 2018). An equivalent linearization method was adopted in their analysis to linearize the inherently nonlinear CID system, the groundwork for which was established in a previous study by Li et al. (2019). Given the benefits of using a CID in a SDOF system, Makris and Moghimi investigated the seismic response of a two-degree-of-freedom (2DOF) structure (Makris and Moghimi 2019). Li and Liang conducted work on CIDs in SDOF and multiple-degree-of-freedom (MDOF) systems for free vibration and harmonic response (Li and Liang 2020). The benefits of incorporating CIDs were subsequently examined experimentally and numerically in SDOF and MDOF steel structures (Málaga-Chuquitaype et al.

2019). Additionally, Thiers-Moggia and Málaga-Chuquitaype proposed the use of CIDs to enhance the seismic performance of rigid and flexible rocking structures and post-tensioned timber structures. They demonstrated that the inclusion of CIDs can effectively reduce seismic rotation demands and improve seismic stability in these structures (Thiers-Moggia and Málaga-Chuquitaype 2020, 2021).

Javidialesaadi and Wierschem have also investigated the CID, which they referred to as the one-directional rotational inertia viscous damper, attached to a linear underlying SDOF system subjected to base excitation (Javidialesaadi and Wierschem 2019). In their study, Javidialesaadi and Wierschem developed a model of the CID dynamics that explicitly considers the damped behavior of the CID flywheels after they become disengaged as well as a modified set of conditions governing the reengagement of the flywheels considering their rotational velocity. The unengaged dynamics of the damped CID flywheels is also similarly adapted in the work by Málaga-Chuquitaype et al. (2019). This is in contrast to many other investigations of the CID, which have assumed that the energy directed to a flywheel of the CID is completely dissipated or harvested after the flywheel stops being engaged (Li and Liang 2020; Makris and Kampas 2016; Moghimi and Makris 2021; Thiers-Moggia and Málaga-Chuquitaype 2019; Wang and Sun 2018; Zheng et al. 2021). This assumption, which is often not valid, has important implications on the system's dynamics and may unduly increase the apparent effectiveness of the CID.

Most previous studies featuring inerters have only considered the elastic behavior of the structures in which they are incorporated. A more recent study of a 2DOF elastic structure with inerters revealed that although the inerters were effective in reducing the first story displacements under certain strong ground motions, the displacements were large enough to suggest that an inelastic model is more appropriate to understand the contribution of an inerter to the deformation of a superstructure (Makris and Moghimi 2019). Based on this, Moghimi and Makris examined the nonlinear seismic response of SDOF and 2DOF yielding structures equipped with an inerter in their first story. The study showed that the apparent elastic period of the structure lengthens in association with an inerter. Moreover, the inerters do not amplify the second story's inelastic response compared to when large values of supplemental damping are used (Moghimi and Makris 2021). Talley et al. also considered nonlinear behavior of the base structure, such as yielding, material, and geometric nonlinearity, in their investigation of the effectiveness of inerter-based dampers to control the seismic response of buildings (Talley et al. 2021).

Although inerter-based dampers have been investigated for the seismic control of structures, studies considering the seismic response of systems employing CIDs are rare. Further work is necessary to assess the response of structures with CIDs when subjected to seismic excitations with varying characteristics to understand if their effectiveness changes with features such as a dominant pulse. Additionally, as most studies on inerter-based devices, including the CID, have considered only the elastic response of structures, the effectiveness of CIDs remains uncertain once material nonlinearity of the base structure (e.g., yielding) initiates.

This study aims to evaluate the seismic performance of the CID considering the damped behavior of the CID flywheels after they become disengaged, inelastic structural behavior, and seismic ground motions with a range of properties. In this numerical study, the CID is incorporated into three different SDOF base structures, each with a nonlinear spring that models yielding and degradation. Incremental dynamic analyses are performed on the structures with a collection of recorded earthquake ground motions until collapse. The collection utilized includes both far-field earthquakes and near-field earthquakes, which more

often include a dominant pulse. The effects of using CIDs with multiple differently sized flywheels are also explored.

The paper is structured as follows. In sect. 2, the equations of motion for the CID installed in a SDOF structure are presented. Section 3 introduces the numerical models of the CID and the SDOF structures featuring nonlinear spring elements that are considered in this work. The incremental dynamic analyses that are performed on the structures are described in Sect. 4 along with the methodology for extracting performance measures from these analyses. The impacts of the CID on yielding and collapse performance are discussed in Sects. 5 and 6, respectively. The behavior of asymmetric CIDs is investigated in Sect. 7. Finally, the observations made in this paper are summarized and conclusions are presented in Sect. 8.

2 Clutch inerter damper (CID)

The CID consists of a passive clutch system, one or more flywheels, and an attachment that is surrounded by a viscous material. The passive clutch engages or disengages depending on the angular velocity of the flywheels. With this clutch, energy is irreversibly transferred away from the main structure to the flywheels.

The concept of the CID is similar to the spinning top toy (see Fig. 1), as described in previous studies (Javidialesaadi and Wierschem 2019; Makris and Moghimi 2019). When the toy's plunger is pushed down, it moves a screw that drives the toy's body, which acts like a flywheel, to rotate in one direction. When the plunger is pulled up, the mechanism disengages, and the flywheel continues to spin freely. This mechanism allows the flywheel to rotate only in one direction, which is similar to ratcheting. When not engaged, the toy's flywheel will spin freely until its motion decays due to the flywheel's own damping. If the plunger is pushed down while the flywheel is spinning, the screw will drive the flywheel

Fig. 1 Spinning top toy, which provides an example of the clutch mechanism in the CID

only if the relative velocity of the plunger is equal to or larger than the linear velocity of the surface at the contact point with the toy's flywheel.

When a flywheel of the CID is engaged, the relative velocity of the structure between the attachment points of the CID and the CID flywheel rotational velocity are related as follows:

$$\dot{\theta} = \frac{2\pi}{\rho}\dot{u}_s \tag{1}$$

where $\dot{\theta}$ represents the rotational velocity of the flywheel, ρ is the lead of the ball-screw, $\dot{u}_s$ is the relative velocity of the structure between the attachment points of the CID. When the CID is attached between a mass and the ground, $\dot{u}_s$ is the velocity of the structure relative to the ground velocity $(\dot{u}_g)$.

When the CID is engaged, the engaged flywheel adds effective mass and damping to the system. Because of the clutch mechanism, energy transferred from the structure to the flywheels cannot be transferred back to the structure. Rather, this energy is dissipated via rotational motion within the viscous material.

In the model considered in this paper, a CID with two flywheels is attached to a mass, as presented in Fig. 2. In this figure, m_s denotes the mass of the main structure, c_s is the assumed inherent viscous damping of the structure, $\ddot{u}_g$ is the ground acceleration, ρ_1 and ρ_2 are the leads of the ball screw, D_1 and D_2 are the damping coefficients of the CID device, and J_1 and J_2 are the moments of inertia of the flywheels. Additionally, the mass is attached to the ground via a nonlinear spring representing the load-deformation response of the structure's lateral force resisting system.

The rotational velocities of the flywheels shown in Fig. 2 are $\dot{\theta}_1$ and $\dot{\theta}_2$. As each of the CID's flywheels can only be engaged in one direction, one flywheel will be engaged

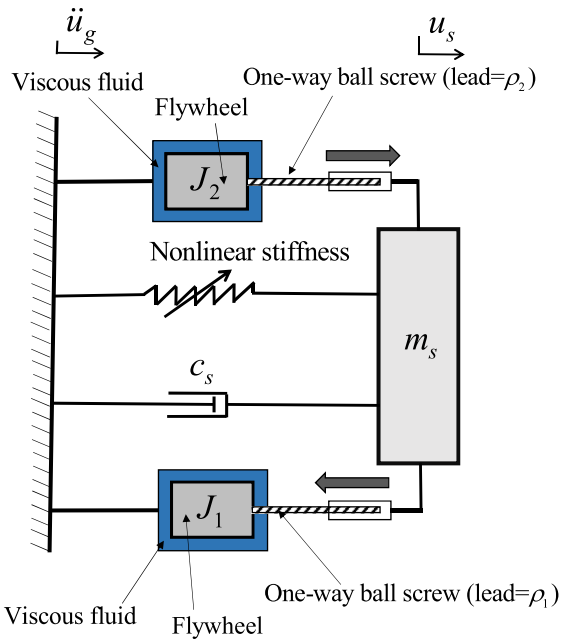

Fig. 2 SDOF main structure with attached CID

with positive velocity of the structure and the other flywheel will be engaged with negative velocity. The equation of motion for the system in Fig. 2 will vary between three different states depending on the kinematics of the system:

State 1: When the structure moves left $\left(\dot{u}_s(t) < 0\right)$ and the relative velocity of the structure is equal to or larger than the linear velocity of the first flywheel at the contact point $\left(|\dot{u}_s(t)| \geq \frac{\rho_1}{2\pi}|\dot{\theta}_1(t)|\right)$, the first flywheel is engaged, and the second flywheel of the CID moves freely. The equations of motion for this state are

$$\begin{aligned} &\left(m_s + J_1\frac{4\pi^2}{\rho_1^2}\right)\ddot{u}_s + \left(c_s + D_1\frac{4\pi^2}{\rho_1^2}\right)\dot{u}_s + F_{ns} = -m_s\ddot{u}_g \\ &J_2\frac{4\pi^2}{\rho_2^2}\ddot{\theta}_2 + D_2\frac{4\pi^2}{\rho_2^2}\dot{\theta}_2 = 0 \end{aligned} \tag{2}$$

In this equation, F_{ns} represents the restoring force from the nonlinear spring in the model. Alternatively, these equations of motion can be presented as

$$\begin{aligned} &\left(m_s + m_{r1}\right)\ddot{u}_s + \left(c_{r1} + c_s\right)\dot{u}_s + F_{ns} = -m_s\ddot{u}_g \\ &m_{r2}\ddot{\theta}_2 + c_{r2}\dot{\theta}_2 = 0 \end{aligned} \tag{3}$$

where

$$m_{r1} = J_1\frac{4\pi^2}{\rho_1^2}\; m_{r2} = J_2\frac{4\pi^2}{\rho_2^2}\; c_{r1} = D_1\frac{4\pi^2}{\rho_1^2}\; c_{r2} = D_2\frac{4\pi^2}{\rho_2^2} \tag{4}$$

State 2: As the structure moves to the right $\left(\dot{u}_s(t) > 0\right)$ and the relative velocity of the structure is equal to or larger than the linear velocity of the second flywheel at the contact point $\left(|\dot{u}_s(t)| \geq \frac{\rho_2}{2\pi}|\dot{\theta}_2(t)|\right)$, the second flywheel is engaged, and the first flywheel of the CID spins freely.

$$\begin{aligned} &\left(m_s + m_{r2}\right)\ddot{u}_s + \left(c_{r2} + c_s\right)\dot{u}_s + F_{ns} = -m_s\ddot{u}_g \\ &m_{r1}\ddot{\theta}_1 + c_{r1}\dot{\theta}_1 = 0 \end{aligned} \tag{5}$$

State 3: The structure oscillates without engaging either of the flywheels when none of the above conditions are met. In this case, both flywheels of the CID spin freely and the system has the following equations of motion.

$$\begin{aligned} &m_s\ddot{u}_s + c_s\dot{u}_s + F_{ns} = -m_s\ddot{u}_g \\ &m_{r1}\ddot{\theta}_1 + c_{r1}\dot{\theta}_1 = 0 \\ &m_{r2}\ddot{\theta}_2 + c_{r2}\dot{\theta}_2 = 0 \end{aligned} \tag{6}$$

In most of the previous research related to the CID, the flywheels of the CID are assumed to be at rest at the beginning of each new cycle of motion (Li and Liang 2020; Makris and Kampas 2016; Moghimi and Makris 2021; Thiers-Moggia and Málaga-Chuquitaype 2019; Wang and Sun 2018; Zheng et al. 2021). In other words, when one flywheel is engaged, the other flywheel is assumed to have zero rotational velocity; thus, one of the flywheels of the CID will reengage with the system with any change in the sign of the structure velocity, no matter the amplitude. This assumption is not always

valid, particularly when considering the rapid changes in motion possible when a system is subjected to seismic ground motions; thus, this assumption is not made in this paper.

3 Numerical model

A numerical model of the SDOF structure that is shown schematically in Fig. 2 was developed to perform the analyses for this study. Variations of the model included cases with the base structure alone (without the CID) and with a standard viscous damper (VD) in lieu of the CID. The model was created in OpenSees v3.3.0 (McKenna et al. 2021). Standard truss elements were used for the nonlinear spring, dashpot, and VD. A custom truss element, implementing the equations in Sect. 2, was developed and used for the CID.

The custom truss element for the CID is a 2-node, 4-degree of freedom element that represents the behavior of both flywheels. Flywheel properties (J, α, and D) can be specified separately for each direction. The element has zero stiffness. The mass and damping provided by the element are non-zero only when in state 1 or 2, i.e., when a flywheel is engaged. Flywheel velocity is tracked using internal state variables; when the flywheels are disengaged, their velocity is damped as per equations (3), (5), and (6). The restoring force of the element in state 1 is

$$F_{r1} = m_{r1}\ddot{u} + c_{r1}\dot{u} \tag{7}$$

where $\ddot{u}$ is the relative acceleration between the nodes and $\dot{u}$ is the relative velocity between the nodes. The restoring force in state 2 is

$$F_{r2} = m_{r2}\ddot{u} + c_{r2}\dot{u} \tag{8}$$

The Ibarra, Medina, and Krawinkler (IMK) bilinear model (Ibarra et al. 2005) was used for the nonlinear spring. Example hysteresis and backbone curves are shown in Fig. 3. The IMK model was chosen because it includes explicit softening of the

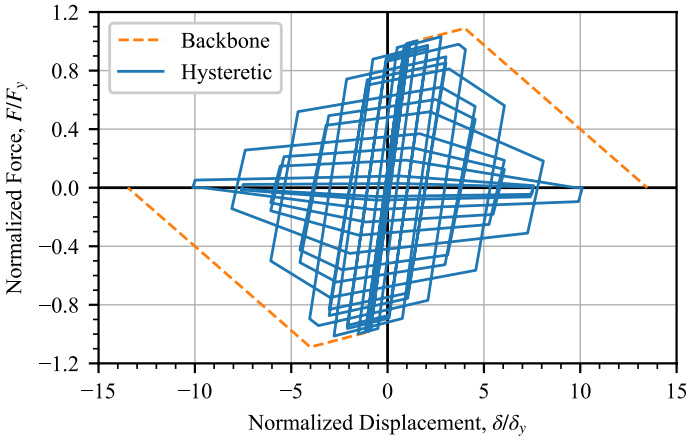

Fig. 3 Example hysteresis and backbone curves of the Ibarra, Medina, and Krawinkler bilinear hysteretic model. $T = 1$ s; other parameters are the same as in Table 1

backbone, stiffness and strength decay in the hysteresis, and has easily evaluable collapse criteria. These features make it ideal for collapse modeling of abstracted SDOF systems. The initial elastic stiffness, k_e, of the structure was defined by the fundamental period, T, and the mass, m_s. The mass and yield strength, F_y, of the structure were selected to be nominal values; normalization of the results, as described later, means that the specific value of these parameters does not impact the results. The Bilin material (Lignos and Krawinkler 2011) was used to implement the IMK bilinear model. Note that the code for the Bilin material was modified in this work to allow output of the internal variable "RSE", which tracks the recoverable strain energy in the material; in this work this is used to find the total energy dissipated by the material as part of the collapse detection procedure described in Sect. 4.

P-Δ effects are included as described by Ibarra and Krawinkler (2005), where a stability coefficient θ modifies the strength and stiffness of the structure, while keeping the yield displacement, δ_y, and capping displacement, δ_c, the same, as shown in Fig. 4. A stability coefficient of 0.015 was used for all analyses.

The structural parameters selected for this study are shown in Table 1. The selected value of ductility capacity is described as "medium" and the hysteretic energy dissipation factors are described as associated with "slow" cyclic deterioration by the model authors (Ibarra and Krawinkler 2005). Further investigation would be necessary to evaluate the variation of the efficacy of the CID with structural parameters other than fundamental period, as this falls outside the scope of the present work.

There are two sources of viscous damping in the model: the structure's inherent damping, and either a CID or VD. The structure's inherent damping, c_s, was kept constant, and defined by

$$c_s = 2\zeta\sqrt{k_e m_s} \tag{9}$$

As described in the previous section, when engaged with negative velocity (i.e., State 1), the CID provides an effective mass, m_{r1}, and effective damping, c_{r1}. When engaged with positive velocity (i.e., State 2), the CID provides effective mass and damping as m_{r2} and c_{r2}, respectively. The "average" effective mass and damping were defined as

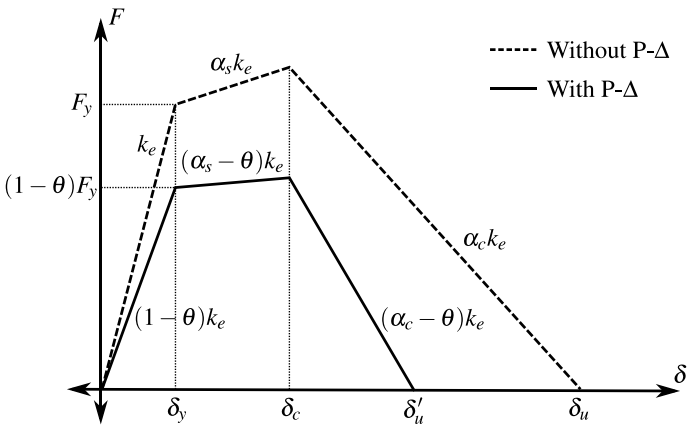

Fig. 4 Backbone curves of the Ibarra, Medina, and Krawinkler model with and without P-Δ effects. Note that δ_y and δ_c are not affected by P-Δ

Table 1 Structure parameters

Symbol	Description	Value(s)
T	Fundamental period [s]	0.5, 1.0, 2.0
m_s	Structure mass [Gg]	1.0
F_y	Yield strength [kN]	1.0
δ_c/δ_y	Ductility capacity	4.0
α_s	Strain-hardening factor	0.05
α_c	Strain-softening factor	−0.10
$\gamma=\gamma_{s,c,k,a}$	Hysteretic energy dissipation factors	100
c	Cyclic deterioration exponent	1.0
λ	Residual strength factor	0.0
ζ	Structure inherent damping, ratio of critical damping	0.01
θ	Stability coefficient	0.015

$$m_r = \frac{1}{2}\left(m_{r1} + m_{r2}\right) \tag{10}$$

$$c_r = \frac{1}{2}\left(c_{r1} + c_{r2}\right) \tag{11}$$

To normalize these average values to the structure, the effective mass ratio was defined by the mass ratio to the structure, m_r/m_s, and the effective damping ratio, ζ_r, was defined as shown below.

$$c_r = 2\zeta_r\sqrt{k_e\left(m_s + m_r\right)} \tag{12}$$

For a symmetric CID, the effective mass and damping are the same in both directions ($m_r=m_{r1}=m_{r2}$ and $c_r=c_{r1}=c_{r2}$). For an asymmetric CID, the level of asymmetry was defined by the ratio AR, which is defined as

$$AR = \frac{m_{r1}}{m_{r1} + m_{r2}} = \frac{c_{r1}}{c_{r1} + c_{r2}} \tag{13}$$

The damping of the VD, c_d, was defined by an effective added damping ratio ζ_d.

$$c_d = 2\zeta_d\sqrt{k_e m_s} \tag{14}$$

Each of the three base structures (i.e., different fundamental periods, see Table 1) was analyzed without modification, with various CIDs, and with various VDs. For the main portion of this work investigating symmetric CIDs, the m_r/m_s values were varied from 0.05 to 1.0 in increments of 0.05 and the ζ_r values were varied from 0.005 to 0.1 in increments of 0.005, resulting in a total of 400 individual CID configurations for each base structure. The value of ζ_d was also varied from 0.005 to 0.1 in increments of 0.005, resulting in a total of 20 individual VD configurations for each base structure. A total of 421 configurations (1 configuration without dampers, 400 with CIDs, and 20 with VDs) were examined for each base structure.

4 Analysis

The main analysis results examined in this work are the ground motion intensities at which yield of the base structure initiates and the ground motion intensities at which collapse occurs. These intensities are computed for each configuration of each base structure using incremental dynamic analysis (Vamvatsikos and Cornell 2002).

Each incremental dynamic analysis was run using the 50 ground motion pairs of the FEMA P695 far-field and near-field record sets, which are representative of far-from-fault and near-fault earthquakes, respectively (FEMA 2009). The near-field record set is divided into ground motions with pulse and ground motions without pulse (14 each). For individual nonlinear response history analyses, ground motions were scaled to a selected relative intensity $(S_a/g)/\eta$ as described by Ibarra et al. (2005), where S_a is the spectral pseudo-acceleration of a 5% damped linear oscillator due to the selected ground motion at the period T of the underling structure without a CID, g is the standard acceleration due to gravity, and η is the yield strength of the structure normalized by the structure's seismic weight (i.e., $\eta = F_y/W$). Results are reported normalized by appropriate structural parameters: force in the structure is normalized by the yield strength F_y, displacement is normalized by the yield displacement δ_y, and energy is normalized by the hysteretic energy dissipation capacity $E_t = \gamma F_y \delta_y$.

When determining the yield intensity for a given ground motion, the relative intensity was incremented by 0.25 until yield was detected. Once detected, a bisecting algorithm was used to determine the yield intensity with a tolerance of 0.01. Yield is considered to have occurred when the absolute displacement of the structure exceeds the yield displacement δ_y.

When determining the collapse intensity for a given ground motion, the relative intensity was incremented by 0.25 until collapse was detected. The intensity at which collapse was detected was recorded as the collapse intensity and no further analyses were performed with that pair of structure and ground motion. Collapse is considered to have occurred when either the reference hysteretic energy dissipation capacity, E_t, has been exhausted, or the backbone curve has been fully traversed and displacement exceeds δ_u (Fig. 4). Both of these conditions cause the stiffness of the structure to be zero, and no further force is generated proportional to the displacement of the structure. Force continues to be generated by the constant inherent damping and the attached damper if present. Since the models in this study have a relatively high energy dissipation capacity ($\gamma = 100$), almost all collapses occurred due to the maximum displacement criterion.

The ground motion intensity at which yield initiates, S_y, or collapse occurs, S_c, is normalized by the same intensity for the structure without a damper installed—S_{y0} and S_{c0}, respectively. These values are termed the normalized yield intensity, $\hat{S}_y$, and the normalized collapse intensity, $\hat{S}_c$, and are defined by

$$\hat{S}_y = S_y / S_{y0} \tag{15}$$

and

$$\hat{S}_c = S_c / S_{c0} \tag{16}$$

The medians of these normalized intensities, notated $\tilde{S}_y$ and $\tilde{S}_c$, are the primary result examined in this work. Also examined is the median absolute deviation, which is analogous

to the standard deviation, but more appropriate for use with medians and more resistant to outliers (Hampel 1974). The computation of these results is shown schematically in Fig. 5.

5 Initial yield

This section presents the findings of a parametric incremental dynamic analysis to determine the median normalized yield intensity, $\tilde{S}_y$, of the SDOF numerical model subjected to the collection of far-field and near-field seismic ground motion sets. Recall that an $\tilde{S}_y$ of 1.5 for a set of CID parameters indicates that half the ground motions show at least a 50% increase in yield intensity for that CID parameter set relative to the no control case. The model parameters included in this parametric analysis are the effective damping ratio (ζ_r), the effective mass ratio (m_r/m_s), and the fundamental period of the underlying structure. Results in this section only consider symmetric CIDs.

Figure 6 shows $\tilde{S}_y$ for the SDOF structure with a CID for a range of effective damping and effective mass ratios. $\tilde{S}_y$ for the structure increases as the effective damping ratio increases for any given effective mass ratio. This result is logical given that the flywheel motion is damped out more quickly at higher effective damping ratios, which dissipates energy faster and allows for the CID to engage with the structure again sooner. In a trend similar to the effective damping ratio, a higher earthquake intensity is necessary to yield the structure as the effective mass ratio increases. As an example, at an effective damping ratio of 0.1, $\tilde{S}_y$ increases from 1.8 for a CID with an effective mass ratio of 0.1 to over

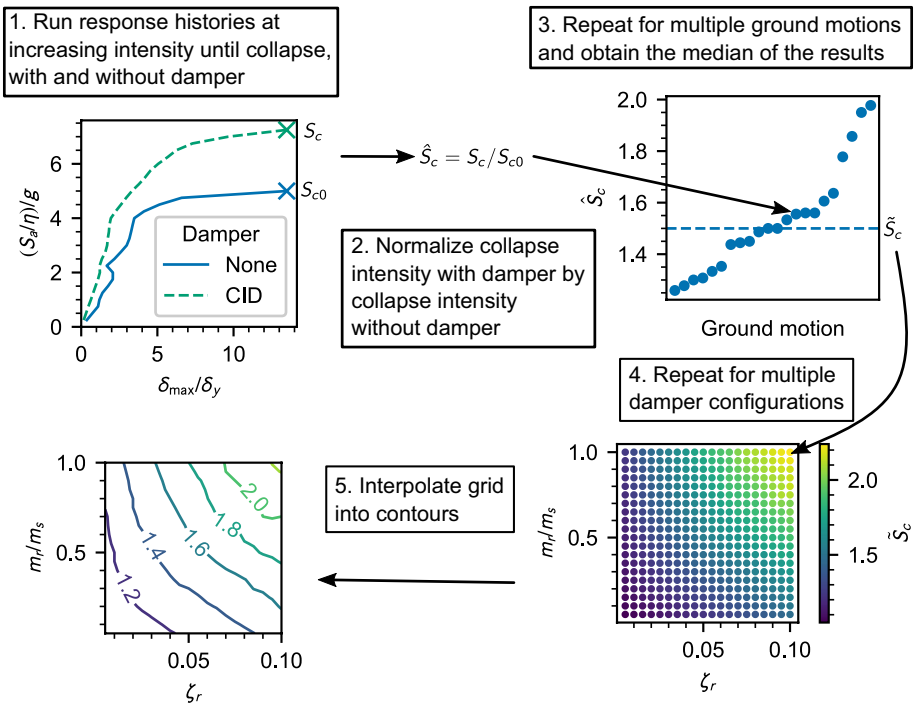

Fig. 5 Process for constructing $\tilde{S}_c$ contour plots from individual ground motion results. A similar process is used to construct $\tilde{S}_y$ contour plots

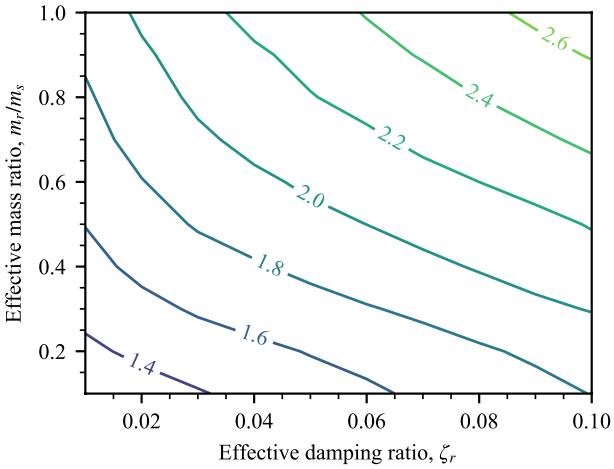

Fig. 6 Contour plot showing $\tilde{S}_y$ for different CID effective mass and damping ratios over all fundamental periods and ground motion sets

2.6 for a CID with an effective mass ratio of 1.0. One reason for this increase in efficacy with higher effective mass ratios is that a higher effective mass ratio increases the amount of energy that can be irreversibly transferred to the CID flywheels at a given structural response amplitude.

In order to investigate the effect of the fundamental structural period on $\tilde{S}_y$, separate $\tilde{S}_y$ are plotted in Fig. 7 for the structures with periods 0.5, 1, and 2 s. Figure 7 shows that, for all structure periods considered, $\tilde{S}_y$ increases with the increasing effective mass ratio and effective damping ratio of the CID, which aligns with the previous results in Fig. 6. Consequently, the system with the highest effective mass ratio and highest effective damping ratio CID yields at a higher median relative earthquake intensity irrespective of the different underlying periods considered.

An alternative means of plotting $\tilde{S}_y$ of the structures with different fundamental periods and different CID parameters is shown in Fig. 8. In this figure, three effective mass ratios (0.1, 0.5, and 1.0) are considered for the CID and $\tilde{S}_y$ is plotted versus the effective damping ratio separately for the three underlying structural periods. From this figure it is easier to observe that $\tilde{S}_y$ is similar for nearly all CID configurations at all of the

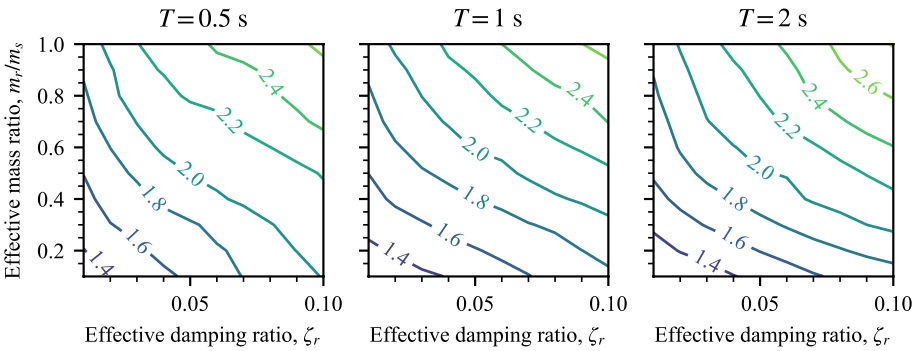

Fig. 7 Contour plots showing effect on $\tilde{S}_y$ of the CID effective mass ratio, CID effective damping ratio, and the period of the underlying structure

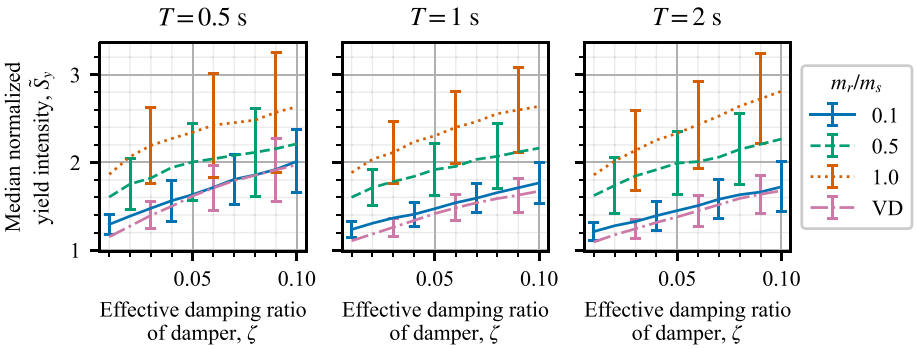

Fig. 8 $\tilde{S}_y$ for different periods of the underlying structure for CID with different effective mass ratios and over a range of CID and VD effective damping ratios. Bars on plots indicate the $\hat{S}_y$ median absolute deviation

examined fundamental periods. The exception to this is that the 0.5 s structural period case outperforms the other cases when the mass ratio is low (0.1). Additionally, the 2 s structural period case outperforms the other cases when the mass ratio is high (1.0) and the damping ratio is on the high end of the range examined. While some differences in $\tilde{S}_y$ exist for different effective mass ratios and structure periods, the rate of change of $\tilde{S}_y$ with increased effective damping remains similar in all cases.

The performance of the structure with a CID can be compared with the performance of the structure with a supplemental VD instead. In Fig. 8, $\tilde{S}_y$ for the SDOF structure equipped with the CID is plotted along with $\tilde{S}_y$ of the same structure where the CID is replaced with a supplemental VD. It is observed that for all the effective mass ratios of the CID considered, $\tilde{S}_y$ of the structure with the CID is higher than the structure with a VD for the same effective damping ratio. Moreover, $\tilde{S}_y$ increases as the effective damping ratios increase for the structure with the CID and the VD. For instance, when the effective damping ratio increases from 0.01 to 0.1, $\tilde{S}_y$ of the structure with the VD increases from about 1.2 to 2.0 with the 0.5 s period structure, while for the same period structure and over the same range of effective damping ratios, $\tilde{S}_y$ of the 1.0 effective mass ratio CID increases from about 1.9 to 2.6.

The effects on $\tilde{S}_y$ for the different ground motion sets, far-field, near-field no pulse, and near-field with pulse are investigated in Fig. 9 for both the CID and the VD. As was also the case with Fig. 8, $\tilde{S}_y$ is higher for any structure with a CID than with a VD for a given effective damping ratio for all of the ground motion sets. Additionally, $\tilde{S}_y$ is the highest for both the VD and the CID when the far-field seismic motion set is applied and lowest for the near-field with pulse set. The superior pre-yield performance when considering the far-field ground motion set may be because the characteristics of this set make it more broadband and less pulse dominated, which allows for a larger number of cycles where the damping devices can be more effective. In the results from all the ground motion sets, $\tilde{S}_y$ increases with a larger effective damping ratio. Although the different ground motion sets have different characteristics, the rate of increase in $\tilde{S}_y$ with increasing effective damping ratio is similar for the different ground motion sets.

To investigate the dispersion of the $\hat{S}_y$ results, the median absolute deviation related to the results in Figs. 8 and 9 are plotted as vertical bars for the CID and VD. From these

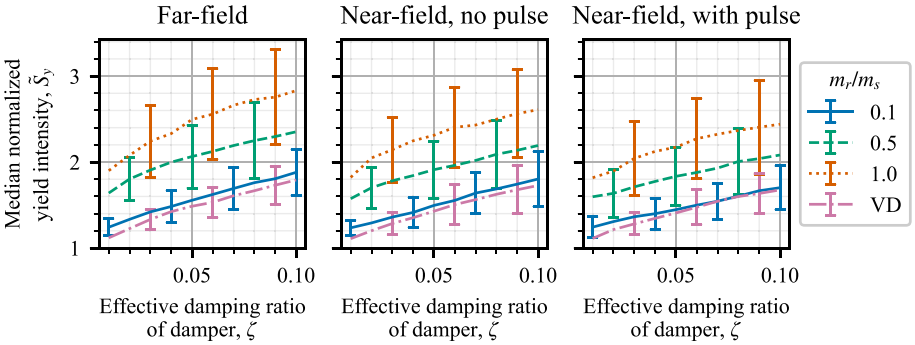

Fig. 9 $\tilde{S}_y$ for different ground motion sets for CID with different effective mass ratios and over a range of CID and VD effective damping ratios. Bars on plots indicate the $\hat{S}_y$ median absolute deviation

$\hat{S}_y$ dispersion results, no discernable trends are evident except that the dispersion of $\hat{S}_y$ increases as the amplitude of $\tilde{S}_y$ increases.

6 Collapse resistance

In this section, the collapse resistance of structures with CIDs is evaluated based on the normalized collapse intensity, $\hat{S}_c$, and median normalized collapse intensity, $\tilde{S}_c$. Recall, $\hat{S}_c$ equals the collapse intensity of the structure with the damper (CID or VD), S_c, divided by the collapse intensity of the structure without the damper, S_{c0}. For this study, the collapse capacity of the SDOF structure is estimated for a range of effective damping ratios (ζ_r), effective mass ratios (m_r/m_s), three fundamental periods (0.5, 1, and 2 s), and three ground motion sets as described in Sect. 4. Results in this section only consider symmetric CIDs.

Figure 10 presents $\tilde{S}_c$ of the SDOF structure for all configurations of the structure and earthquake ground motions sets. Each line in the contour plot indicates the effectiveness of the CID in collapse resistance in comparison to a no control case where the structure does not have a CID or VD attached. For example, a value of 1.5 for a set of CID parameters indicates that half the ground motions show at least a 50% increase in collapse intensity for that CID parameter set relative to the no control case. Note that all structures analyzed, even in the no control case, have some inherent damping. $\tilde{S}_c$ increases with both increases in the effective damping and effective mass ratio. However, with lower levels of damping, the performance gains with increasing effective mass ratio are minor. Similarly, the performance gains are less significant with lower effective mass ratios. Nevertheless, the maximum $\tilde{S}_c$ with a low effective mass ratio is greater than that with a low effective damping ratio. When the effective mass ratio is 0.2 and effective damping ratios range from about 0.02 to 0.1, $\tilde{S}_c$ increases from about 1.2 to 1.6. Alternatively, $\tilde{S}_c$ increases from about 1.2 to 1.4 when the effective damping ratio is 0.02 and effective mass ratios range from 0.2 to 1. This decreased sensitivity to the effective mass ratio at low levels of effective damping could be because at a low level of effective damping, the device takes a much longer time to dissipate enough rotational kinetic energy to become able to effectively engage with the structure again. Conversely, with high effective damping and larger effective mass, large amounts of energy may be directed to the device's flywheels at any given time, and

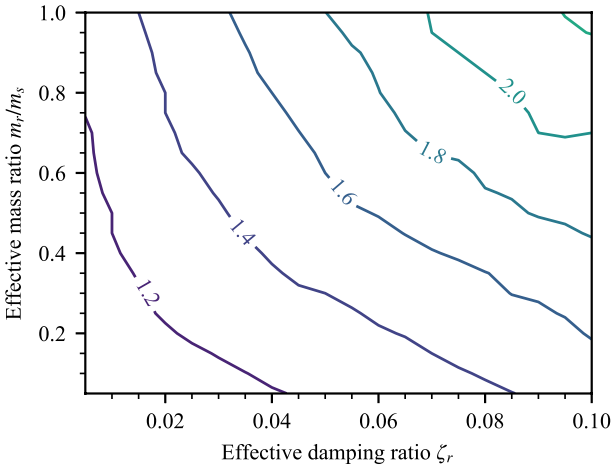

Fig. 10 Contour plot showing $\tilde{S}_c$ for different effective mass and damping ratios over all fundamental periods and ground motion sets

this energy is dissipated rapidly allowing the CID to be able to quickly engage with the response of the structure again.

The results in Figs. 6 and 10 can be contrasted to compare the yield and collapse performance of the CID, as measured by $\tilde{S}_y$ and $\tilde{S}_c$, and the differences in how the performance changes when the CID parameters are varied. The minimum and maximum values of $\tilde{S}_y$ observed are about 1.3 and 2.6, while the minimum and maximum values of $\tilde{S}_c$ observed are about 1.1 and 2.2. When the effective mass is 0.1, $\tilde{S}_y$ varies from about 1.3 to 1.8 and $\tilde{S}_c$ varies from about 1.1 to 1.5. When the effective damping is 0.01, $\tilde{S}_y$ varies from about 1.3 to 1.9 and $\tilde{S}_c$ varies from about 1.1 to 1.3. These results show that the relative performance of the CID decreases when considering collapse rather than yield. Furthermore, these results show that the decrease in collapse performance is more prevalent in the low effective damping case, compared to the low effective mass ratio case. These results are consistent with the fact that before yielding the only damping in the no control case comes from a small amount of inherent viscous damping, but after yielding significant energy dissipation results from the structures' hysteresis. As the structure itself contributes more to its collapse performance than its yield performance, the change in collapse performance due to the CID (which is still significant) is less, particularly when low effective damping inhibits the performance of the CID.

The influence of the effective damping ratio on the engagement of the flywheels is illustrated in Fig. 11. This figure presents the normalized displacement of the SDOF structure under a particular earthquake ground motion, the energy in the flywheels, and energy dissipated by the flywheels. The applied ground motion time-history is also presented in this figure. For this analysis, effective damping ratios of 0.01 and 0.1 are considered as low damping and high damping, respectively. The sharp rises in the flywheel energy in this plot indicate when the flywheels of the CID are engaged. The decreases in flywheel energy occur due to the flywheels' damping when they are spinning freely. The decrease in flywheel energy is faster for the high damping than the low damping case. This faster decrease in flywheel energy typically allows the flywheels in the low damping case to reengage at much lower levels of energy and thus reengage with the system at lower response velocities. While the decrease in flywheel energy is faster for the high damping case, the maximum flywheel energy is higher in the low damping case. The reason for this is that

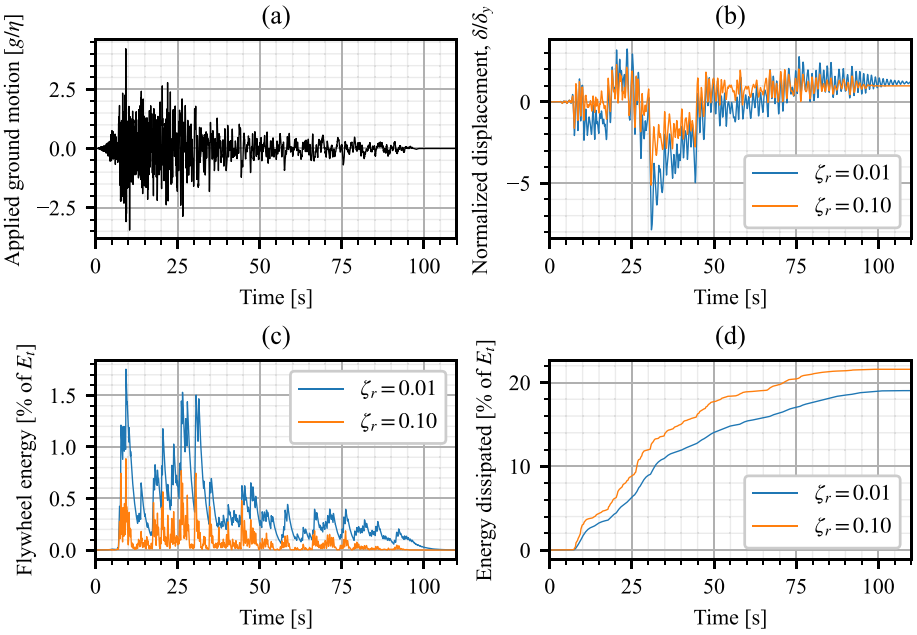

Fig. 11 Example time-history loading and response of CID-equipped structure for two different damping levels. **a** Ground motion time-history; **b** Normalized displacement of the SDOF structure; **c** Flywheel energy; and **d** Total energy dissipated by the flywheels in response to the applied ground motion. Analysis parameters: $T = 1.0$ s, $\eta = 0.000102$, $m_r/m_s = 0.50$, $(S_a/g)/\eta = 5.75$

the CID with low damping is less effective at controlling the response of the structure; thus, the structure with the CID with low damping has a higher response and at this higher response the CID are once again able to be engaged.

$\tilde{S}_c$ of structures with different fundamental periods (of the underlying structure) are separately plotted in Fig. 12 to investigate the effect of the underlying period of the structure on the CID collapse resistance performance relative to the no control case. Once again, all three ground motion sets were considered together for this analysis. The

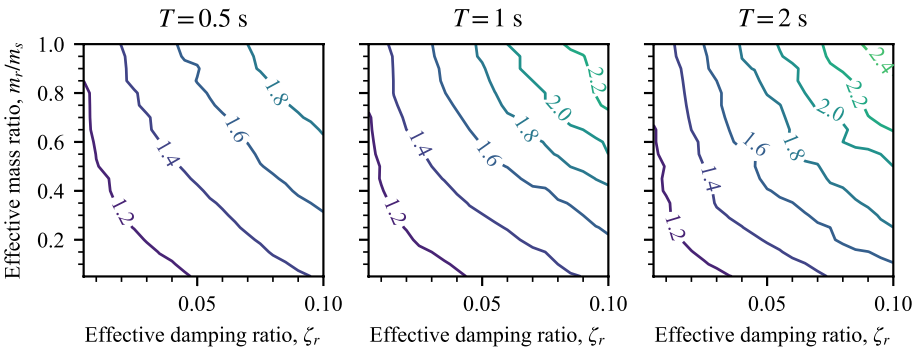

Fig. 12 Contour plots showing effect on $\tilde{S}_c$ of the CID effective mass ratio, CID effective damping ratio, and the period of the underlying structure

overall behavior of collapse resistance remains similar for all the different periods; that is, $\tilde{S}_c$ increases with increasing effective damping and effective mass ratios. Moreover, a general trend to higher $\tilde{S}_c$ is observed with growing periods. For instance, when the fundamental period of the underlying structure is 0.5 s, $\tilde{S}_c$ can reach a maximum of about 1.9 by varying the CID parameters. In contrast, the maximum $\tilde{S}_c$ is about 2.4 with the same set of CID parameters when the underlying period of the structure is 2 s.

An alternative means of plotting $\tilde{S}_c$ of the structures with different fundamental periods and different CID parameters is shown in Fig. 13. From this figure it is easier to observe that $\tilde{S}_c$ is lower for nearly all CID configurations at the shorter fundamental period compared to $\tilde{S}_c$ with the same CID configurations at relatively longer periods.

Figure 13 can also be utilized to investigate the performance of the CID compared to the VD at different damper configurations and with different structure periods. This figure shows that, given a level of effective damping, the CID always outperforms the VD in terms of $\tilde{S}_c$; however, $\tilde{S}_c$ for the CID with effective mass ratio of 0.1 is very similar to $\tilde{S}_c$ for the VD for all of the structure periods considered. Furthermore, this figure shows that while $\tilde{S}_c$ of both the CID and VD increase with increasing effective damping, $\tilde{S}_c$ with the CID can increase much more than with the VD. For example, with the 2 s period structure, $\tilde{S}_c$ for the VD increases from about 1.1 to 1.5 when the effective damping ratio increases from 0.02 to 0.1, while over the same effective damping ratios $\tilde{S}_c$ for the 1.0 effective mass ratio CID increases from about 1.5 to 2.5.

Figure 14 compares $\tilde{S}_c$ for different damper configurations when the structures are subjected to far-field, near-field without pulse, and near-field with pulse ground motion sets separately. Data from all three structure periods was combined together for this analysis. In general, some of the trends observed before are seen here in the results from each ground motion set: $\tilde{S}_c$ increases with increasing effective mass ratio and effective damping, the CID outperforms the VD at any given level of effective damping, but the VD and CID have similar $\tilde{S}_c$ when the effective mass ratio is 0.1. This figure shows that, in terms of $\tilde{S}_c$, the performance of the CID is similar for the different ground motion sets and no clear trends exist that show the CID is able to have consistently better relative collapse performance when subjected to one of the ground motion sets. For example, the CID with an effective mass ratio of 1 has a generally higher $\tilde{S}_c$ for the far-field set,

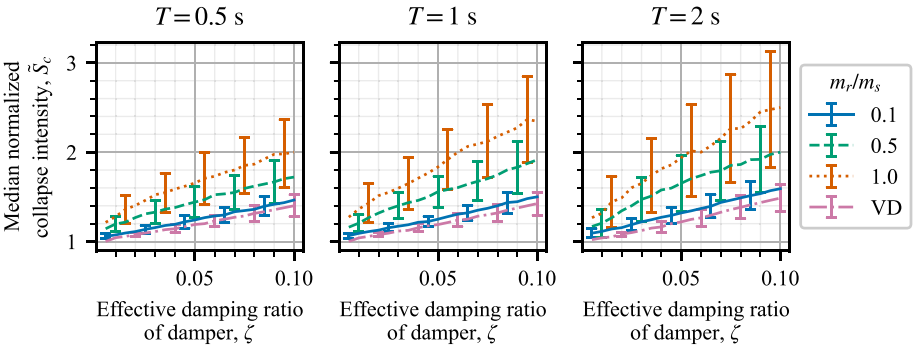

Fig. 13 $\tilde{S}_c$ for different periods of the underlying structure for CID with different effective mass ratios and over a range of CID and VD effective damping ratios. Bars on plots indicate the $\hat{S}_c$ median absolute deviation

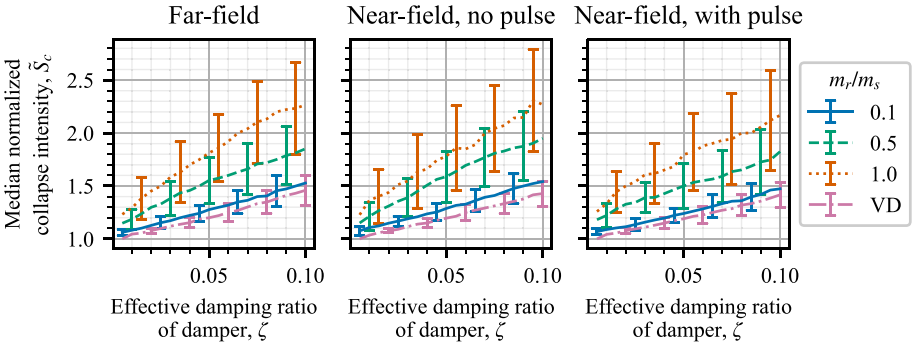

Fig. 14 $\tilde{S}_c$ for different ground motion sets for CIDs with different effective mass ratios and over a range of CID and VD effective damping ratios. Bars on plots indicate the $\tilde{S}_c$ median absolute deviation

but the CID with an effective mass ratio of 0.5 has a generally higher $\tilde{S}_c$ for the near-field without pulse set.

To investigate the dispersion of the $\tilde{S}_c$ results, the median absolute deviation of the results in Figs. 13 and 14 are plotted as vertical bars for the CID and VD. From these $\tilde{S}_c$ dispersion results, no discernable trends are evident except that the dispersion of $\tilde{S}_c$ increases as the amplitude of $\tilde{S}_c$ increases.

7 Asymmetric CIDs

While previous sections have examined symmetric CIDs where the effective mass and the effective damping provided by the CID are the same in both directions, this section considers the behavior that results when the CID is asymmetric. This asymmetry may be present in the CID unintentionally due to malfunctions or manufacturing errors or intentionally in order to produce a CID design that has different natural frequencies when the different flywheels are engaged. In this section, asymmetry in the effective mass and effective damping of the CID is investigated considering different levels of asymmetry (Eq. (13)) ranging from 0.4 to 0.6 ($AR = 0.5$ for symmetric CIDs). $\tilde{S}_c$ of the SDOF structure is evaluated for this range of AR, effective damping ratios $\left(\zeta_r\right)$ ranging from 0.01 to 0.10, and different seismic records.

$\tilde{S}_c$ of the SDOF structures with CIDs with an effective mass ratio of 0.5 and having various effective damping ratios and values of AR is presented in Fig. 15. Additionally, $\tilde{S}_c$ of the SDOF structures with CIDs with an effective damping ratio of 0.05 and having various effective mass ratios and values of AR is presented in Fig. 16. In Figs. 15 and 16, $\tilde{S}_c$ associated with different AR values for the CIDs is presented, including $AR = 0.5$; therefore, these figures can be used to contrast the effectiveness of the symmetric and the asymmetric CIDs in increasing $\tilde{S}_c$. In these figures, $\tilde{S}_c$ increases with increasing effective mass and effective damping ratios for all the AR values. It is evident from Figs. 15 and 16 that, for any given total effective mass and effective damping ratio, the symmetric CID ($AR = 0.5$) is more effective in improving $\tilde{S}_c$. Furthermore, the effectiveness of the CID decreases with increasing asymmetry. However, for low effective damping ratios, the asymmetry has a minor effect on the performance. In all the cases, $\tilde{S}_c$ is greater than unity, indicating that

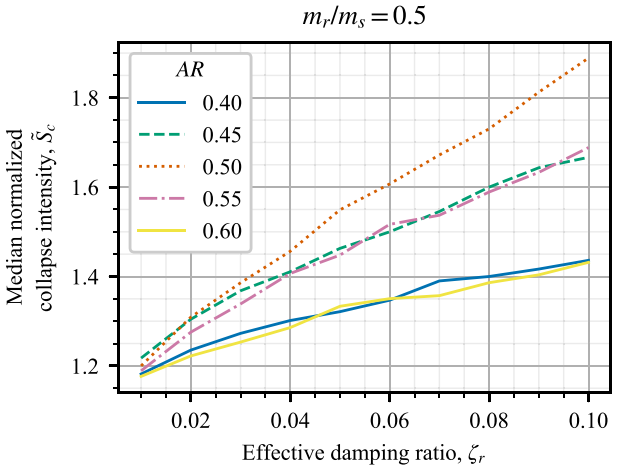

Fig. 15 $\tilde{S}_c$ of the SDOF structures equipped with CID for various *AR* and effective damping ratios given an effective mass ratio of 0.5

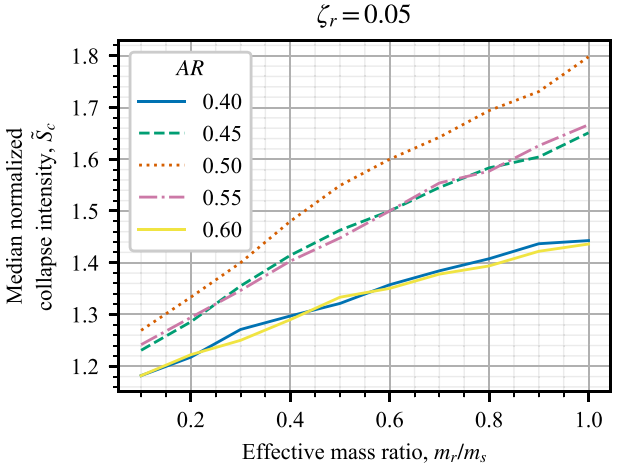

Fig. 16 $\tilde{S}_c$ of the SDOF structures equipped with CID for various *AR* and effective mass ratios given an effective damping ratio of 0.05

the median of the collapse performance of the structure with the CID exceeds the collapse performance of the structure without any damper.

Figure 17 shows $\tilde{S}_c$ of the SDOF structures equipped with CIDs of various *AR* values and is presented such that the effects on $\tilde{S}_c$ of the effective damping ratio and the ground motion set can be investigated. When the effective damping ratio is low, there are only minor changes in $\tilde{S}_c$ between the symmetric and asymmetric CIDs for all the ground motion sets. However, the symmetric CIDs have a greater $\tilde{S}_c$ than the asymmetric CIDs in nearly all cases at higher levels of effective damping for all three ground motion sets. Furthermore, at any given level of effective damping and AR value, the difference in $\tilde{S}_c$ for

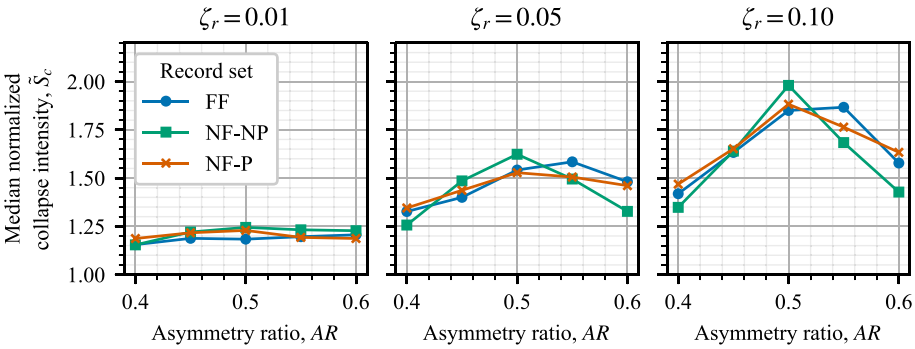

Fig. 17 $\tilde{S}_c$ of the SDOF structure given CID with a range of AR values and different effective damping ratios, comparing response to different ground motion record sets. FF: far-field; NF-NP: near-field, no pulse; NF-P: near-field, with pulse

the different ground motion sets is relatively minor. Note that while some differences in $\tilde{S}_c$ shown in Fig. 17 exist for complimentary AR values (0.4/0.6 or 0.45/0.55), the authors expect that with large enough sets of ground motions, the same $\tilde{S}_c$ would result at these complimentary AR values.

8 Conclusions

The clutch inerter damper (CID) is an innovative device with great potential for passive control of structures. Through numerical analysis of SDOF systems, this work explored the effectiveness of CIDs to mitigate damage and improve the safety of structures subjected to strong earthquake ground motions. The unique features of this study were that this seismic performance was evaluated considering the damped behavior of the CID flywheels after they become disengaged, inelastic structural behavior, seismic ground motions with a range of properties, and asymmetry in the CID. The following was observed from the analyses regarding the performance of CIDs:

- The ability of the CID to protect the structure against yield and collapse increased with increases in effective mass and effective damping of the CID.
- The ability of the CID to protect the structure against yield was greater than its ability to protect the structure against collapse since the CID was the dominant source of energy dissipation in the elastic range while the structure itself contributed significant energy dissipation at the collapse level.
- CIDs with lower effective damping provided less protection against yield and collapse, in part because their flywheels were unable to slow down quickly. With lower damping, the CID less frequently engage effectively with the structure.
- CIDs outperformed viscous dampers with the same effective damping ratio over the entire range of effective masses investigated.
- The performance of the CID was largely similar across the sets of earthquake records utilized (far-field, near-field no pulse, and near-field with pulse); however, the CID was best able to protect the structures against yield for the far-field set.

- The performance of the CID was largely similar across the sets of underlying structure periods considered (0.5, 1, and 2 s); however, against collapse, the CID was best able to protect the structure with 2 s period.
- Asymmetric CIDs typically underperform with respect to symmetric CIDs with the same total effective mass. The performance decreases as the level of asymmetry increases. At lower levels of effective damping, the asymmetry did not change the performance much.

Based on these observations, it is clear that the clutch inerter damper is capable of protecting structures against yielding and collapse and otherwise mitigating the effects of a wide range of types of seismic excitations. Consequently, further investigation on the use of the CID, particularly the symmetric CID, for passive control of structures subjected to seismic excitation is warranted.

Author contributions PCT: Methodology, Software, Investigation, Writing—Reviewing and Editing. ATS: Writing—Original Draft, Reviewing and Editing. NEW: Writing—Reviewing and Editing, Supervision, Conceptualization. MDD: Writing—Reviewing and Editing, Supervision, Conceptualization, Software.

Funding This material is based upon work supported by the National Science Foundation under Grant No. 1944513. Any opinions, findings, and conclusions or recommendations expressed in this material are those of the authors and do not necessarily reflect the views of the National Science Foundation.

Declarations

Conflict of interest The authors declare that they have no conficts of interest.

References

Asai T, Watanabe Y (2017) Outrigger tuned inertial mass electromagnetic transducers for high-rise buildings subject to long period earthquakes. Eng Struct 153:404–410. https://doi.org/10.1016/j.engstruct.2017.10.040

Di Egidio A, Pagliaro S, Fabrizio C (2021) Combined use of rocking walls and inerters to improve the seismic response of frame structures. J Eng Mech 147(5):04021016. https://doi.org/10.1061/(ASCE)EM.1943-7889.0001920

FEMA (2009) Quantification of building seismic performance factors. Federal Emergency Management Agency

Garrido H, Curadelli O, Ambrosini D (2013) Improvement of tuned mass damper by using rotational inertia through tuned viscous mass damper. Eng Struct 56:2149–2153. https://doi.org/10.1016/j.engstruct.2013.08.044

Hampel FR (1974) The influence curve and its role in robust estimation. J Am Stat Assoc 69(346):383–393

Hu Y, Chen MZQ (2015) Performance evaluation for inerter-based dynamic vibration absorbers. Int J Mech Sci 99:297–307. https://doi.org/10.1016/j.ijmecsci.2015.06.003

Hwang J-S, Kim J, Kim Y-M (2007) Rotational inertia dampers with toggle bracing for vibration control of a building structure. Eng Struct 29(6):1201–1208. https://doi.org/10.1016/j.engstruct.2006.08.005

Ibarra LF, Krawinkler H (2005) Global collapse of frame structures under seismic excitations. Stanford University, Stanford

Ibarra LF, Medina RA, Krawinkler H (2005) Hysteretic models that incorporate strength and stiffness deterioration. Earthq Eng Struct Dyn 34(12):1489–1511. https://doi.org/10.1002/eqe.495

Ikago K, Saito K, Inoue N (2012) Seismic control of single-degree-of-freedom structure using tuned viscous mass damper: the tuned viscous mass damper. Earthq Eng Struct Dyn 41(3):453–474. https://doi.org/10.1002/eqe.1138

Javidialesaadi A, Wierschem NE (2019) Energy transfer and passive control of single-degree-of-freedom structures using a one-directional rotational inertia viscous damper. Eng Struct 196:109339. https://doi.org/10.1016/j.engstruct.2019.109339

Lazar IF, Neild SA, Wagg DJ (2014) Using an inerter-based device for structural vibration suppression: using an inerter-based device for structural vibration suppression. Earthq Eng Struct Dyn 43(8):1129–1147. https://doi.org/10.1002/eqe.2390

Li L, Liang Q (2020) Seismic assessment and optimal design for structures with clutching inerter dampers. J Eng Mech 146(4):04020016. https://doi.org/10.1061/(ASCE)EM.1943-7889.0001732

Li L, Liang Q, Qin H (2019) Equivalent linearization methods for a control system with clutching inerter damper. Appl Sci 9(4):688. https://doi.org/10.3390/app9040688

Lignos DG, Krawinkler H (2011) Deterioration modeling of steel components in support of collapse prediction of steel moment frames under earthquake loading. J Struct Eng 137(11):1291–1302. https://doi.org/10.1061/(ASCE)ST.1943-541X.0000376

Ma R, Bi K, Hao H (2021) Inerter-based structural vibration control: a state-of-the-art review. Eng Struct 243:112655. https://doi.org/10.1016/j.engstruct.2021.112655

Makris N, Kampas G (2016) Seismic protection of structures with supplemental rotational inertia. J Eng Mech 142(11):04016089. https://doi.org/10.1061/(ASCE)EM.1943-7889.0001152

Makris N, Moghimi G (2019) Displacements and forces in structures with inerters when subjected to earthquakes. J Struct Eng 145(2):04018260. https://doi.org/10.1061/(ASCE)ST.1943-541X.0002267

Málaga-Chuquitaype C, Menendez-Vicente C, Thiers-Moggia R (2019) Experimental and numerical assessment of the seismic response of steel structures with clutched inerters. Soil Dyn Earthq Eng 121:200–211. https://doi.org/10.1016/j.soildyn.2019.03.016

McKenna F, Fenves GL, Filippou FC, Contributors (2021) Open system for earthquake engineering simulation. University of California, Berkeley

Moghimi G, Makris N (2021) Seismic response of yielding structures equipped with inerters. Soil Dyn Earthq Eng 141:106474. https://doi.org/10.1016/j.soildyn.2020.106474

Smith MC (2002) Synthesis of mechanical networks: the inerter. IEEE Trans Autom Control 47(10):1648–1662. https://doi.org/10.1109/TAC.2002.803532

Smith MC (2020) The inerter: a retrospective. Annu Rev Control Robot Auton Syst 3(1):361–391. https://doi.org/10.1146/annurev-control-053018-023917

Sugimura Y, Goto W, Tanizawa H, Saito K, Ninomiya T, Nagasaku T (2012) Response control effect of steel building structure using tuned viscous mass damper. In: Proc. 15th World Conf. Earthq. Eng. Lisbon, Portugal

Talley PC, Javidialesaadi A, Wierschem NE, Denavit MD (2021) Evaluation of steel building structures with inerter-based dampers under seismic loading. Eng Struct 242:112488. https://doi.org/10.1016/j.engstruct.2021.112488

Thiers-Moggia R, Málaga-Chuquitaype C (2019) Seismic protection of rocking structures with inerters. Earthq Eng Struct Dyn 48(5):528–547. https://doi.org/10.1002/eqe.3147

Thiers-Moggia R, Málaga-Chuquitaype C (2020) Seismic control of flexible rocking structures using inerters. Earthq Eng Struct Dyn 49(14):1519–1538. https://doi.org/10.1002/eqe.3315

Thiers-Moggia R, Málaga-Chuquitaype C (2021) Performance-based seismic design and assessment of rocking timber buildings equipped with inerters. Eng Struct 248:113164. https://doi.org/10.1016/j.engstruct.2021.113164

Vamvatsikos D, Cornell CA (2002) Incremental dynamic analysis. Earthq Eng Struct Dyn 31(3):491–514. https://doi.org/10.1002/eqe.141

Wagg DJ (2021) A review of the mechanical inerter: historical context, physical realisations and nonlinear applications. Nonlinear Dyn 104(1):13–34. https://doi.org/10.1007/s11071-021-06303-8

Wang M, Sun F (2018) Displacement reduction effect and simplified evaluation method for SDOF systems using a clutching inerter damper. Earthq Eng Struct Dyn 47(7):1651–1672. https://doi.org/10.1002/eqe.3034

Wang F-C, Hong M-F, Chen C-W (2010) Building suspensions with inerters. Proc Inst Mech Eng Part C J Mech Eng Sci 224(8):1605–1616. https://doi.org/10.1243/09544062JMES1909

Zhao Z, Zhang R, Wierschem NE, Jiang Y, Pan C (2021) Displacement mitigation–oriented design and mechanism for inerter-based isolation system. J Vib Control 27(17 18):1991–2003. https://doi.org/10.1177/1077546320951662

Zheng Y-L, Li L-Y, Zhang T-J (2021) Energy analysis and optimization of inerter-based systems. J Vib Control 28(9 10):985–997. https://doi.org/10.1177/1077546320987730